

Quantitative analysis of three-dimensional biological cells using interferometric microscopy

Natan T. Shaked^{1*} and Adam Wax²

¹ Department of Biomedical Engineering, Faculty of Engineering, Tel Aviv University
Ramat Aviv 69978, Israel
*nshaked@tau.ac.il

² Department of Biomedical Engineering, Fitzpatrick Institute for Photonics, Duke University
Durham, North Carolina 27708, USA.

ABSTRACT

Live biological cells are three-dimensional microscopic objects that constantly adjust their sizes, shapes and other biophysical features. Wide-field digital interferometry (WFDI) is a holographic technique that is able to record the complex wavefront of the light which has interacted with *in-vitro* cells in a single camera exposure, where no exogenous contrast agents are required. However, simple quasi-three-dimensional holographic visualization of the cell phase profiles need not be the end of the process. Quantitative analysis should permit extraction of numerical parameters which are useful for cytology or medical diagnosis. Using a transmission-mode setup, the phase profile represents the multiplication between the integral refractive index and the thickness of the sample. These coupled variables may not be distinct when acquiring the phase profiles of dynamic cells. Many morphological parameters which are useful for cell biologists are based on the cell thickness profile rather than on its phase profile. We first overview methods to decouple the cell thickness and its refractive index using the WFDI-based phase profile. Then, we present a whole-cell-imaging approach which is able to extract useful numerical parameters on the cells even in cases where decoupling of cell thickness and refractive index is not possible or desired.

Keywords: Cell analysis, interference microscopy, phase holography.

1. INTRODUCTION

Wide-field digital interferometry (WFDI) is a label-free holographic technique that is able to record the entire complex wavefront of the light interacted with a sample [1]. For optically transparent sample, such as biological cell *in vitro*, one can obtain full quantitative phase profiles, as well as correct for out-of-focus image features by post-processing. Alternative methods include using fluorescent dyes or other exogenous contrast agents (which might suffer from cytotoxicity and photobleaching problems), or other label free methods like phase contrast microscopy and differential interference contrast (DIC) microscopy (which suffer from not being inherently quantitative, preventing straightforward extraction of the entire phase profile of the cell as possible by WFDI).

WFDI microscopy (also called digital holographic microscopy) has been applied to various types of biological cell systems and has recorded a diverse range of cellular phenomena [2-10].

Although WFDI is a quantitative recording technique, simple quasi-three-dimensional holographic visualization of the cell phase profile need not be the end of the process. Quantitative analysis should permit extraction of numerical parameters which are useful for biological research or medical diagnosis. Using a transmission-mode interferometric setup, the resulting phase profile represents the optical path delay (OPD) profile, defined as the multiplication between the refractive index differences and the thickness of the sample. These coupled parameters, the refractive index and the thickness, are not distinct when acquiring the phase profile of a dynamic cell. To allow quantitative cell analysis by

WFDI, this fact must be considered during the system development and the following quantitative data analysis. Many morphological parameters which are useful for cell biologists (such as cell volume, cell force distribution, etc.) are based on the physical thickness profile of the cell rather than on its phase profile. Therefore, we review methods to decouple the cell thickness from refractive index using the cell phase profile obtained by WFDI.

For certain cells, such as red blood cells (RBCs), in which a constant refractive index can be assumed for the entire cell contents, the thickness profile can be directly obtained from the phase profile. In contrast, for other types of cells, containing inner organelles with different refractive indices such as cell nuclei and mitochondria, certain parameters such as dry-mass and relative volume can be obtained directly from the phase profile under reasonable assumptions.

Alternatively, full decoupling of the cell refractive index and its thickness can be accomplished by measuring the phase profiles of the same cell immersed in two different growth media with distinct refractive indices. In addition, when the thickness profile is measured by another method (such as confocal microscopy), it is possible to calculate the refractive index of the cell inner organelles. These methods, however, are not useful for highly dynamic cells.

We finally show that the phase profile is still useful for quantitative analysis of cells even in cases where decoupling of thickness and refractive index is not possible or desired. This is carried out by defining new numerical phase-profile-based parameters, which can uniquely characterize certain cell processes of interest.

2. BASIC PRINCIPLES OF PHASE MEASUREMENTS BY WFDI

A possible scheme of off-axis WFDI setup is presented in Fig. 1(a) [11]. This specific setup is based on Mach-Zehnder interferometer and an off-axis holographic geometry. Light from a coherent source is first spatially filtered using a pair of spherical lenses and a confocally-positioned pinhole, and then split into reference and object beams by beam splitter BS₁. The object beam is transmitted through the sample and magnified by a microscope objective. The reference beam is transmitted through a compensating microscope objective (typically similar to the object-beam objective) and then combined with the object beam at an angle. The combined beams are projected onto a digital camera by lens L₂, where the distance between each of the microscope objectives and lens L₂ is equal to the summation of their focal lengths. This configuration allows projection of the amplitude and phase distribution of the sample onto the camera. The combination of the sample and reference beams creates a high-spatial-frequency off-axis hologram of the sample on the camera.

Figure 1(b) presents the chamber in detail. As can be seen in this figure, the cell is typically adhered to the bottom coverslip and is immersed in cell growth medium. The spatially-varying phase measured by WFDI is proportional to the OPD profile of the sample and defined as follows:

$$\begin{aligned}\phi(x, y) &= \frac{2\pi}{\lambda} [\bar{n}_c(x, y) h_c(x, y) + n_m(h_m - h_c(x, y))] \\ &= \frac{2\pi}{\lambda} [(\bar{n}_c(x, y) - n_m) h_c(x, y) + n_m h_m] \\ &= \frac{2\pi}{\lambda} [OPD_c(x, y) + OPD_m],\end{aligned}\quad (1)$$

where λ is the illumination wavelength, $\bar{n}_c(x, y)$ is the spatially varying integral refractive index, n_m is the medium refractive index, $h_c(x, y)$ is the spatially varying thickness profile of the cell, and h_m is the thickness of the cell medium. Per spatial point (x, y) , the integral refractive index \bar{n}_c is defined as follows [12]:

$$\bar{n}_c = \frac{1}{h_c} \int_0^{h_c} n_c(z) dz, \quad (2)$$

where $n_c(z)$ is a function representing the intracellular refractive index along the cell thickness. The value of $OPD_m = n_m h_m$ can be measured in advance in places where there are no cells located, and then subtracted from the total OPD measurement. However, $OPD_c = (\bar{n}_c(x, y) - n_m) h_c(x, y)$ contains two coupled parameters: the integral refractive index profile of the cell and the cell thickness profile (under the assumption that n_m is known). These parameters might not be distinct when acquiring the phase profile of a dynamic cell, and this fact must be considered during development of the WFDI optical system capturing the cell phase profile and in the quantitative data analysis that follows.

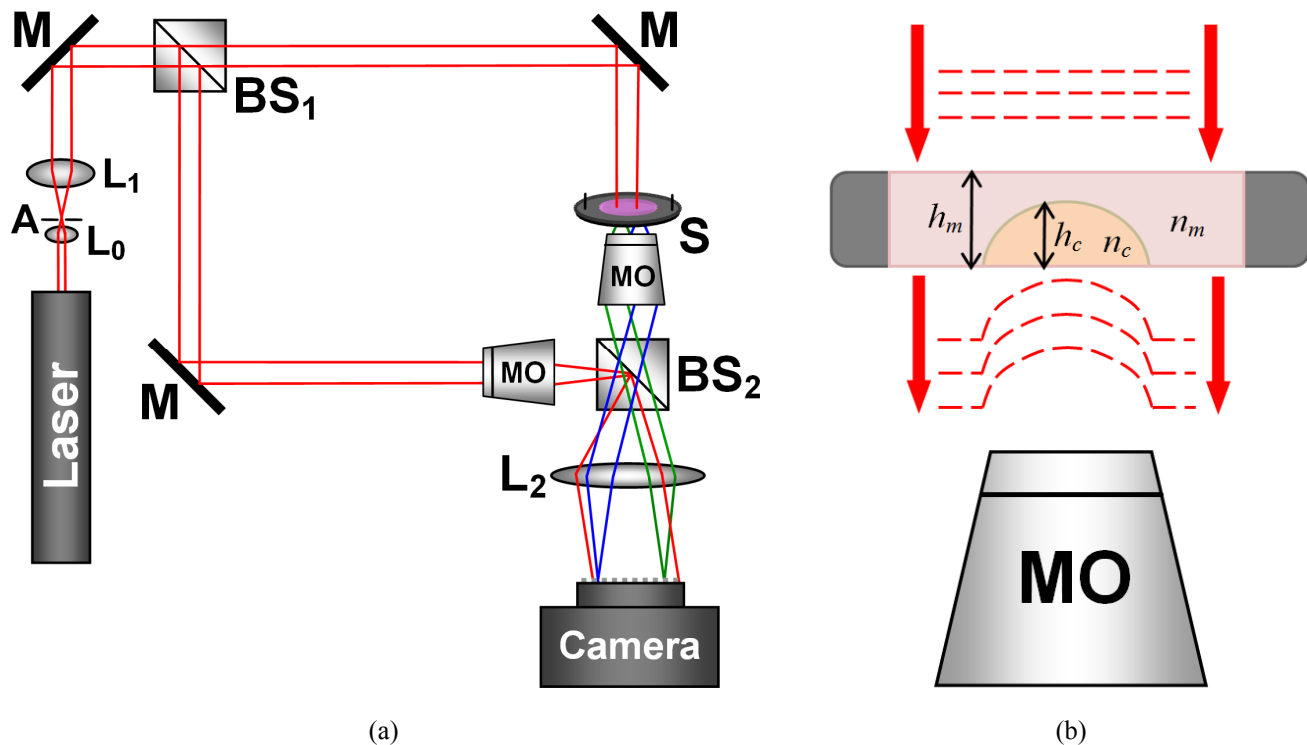


Fig. 1. (a) Off-axis WFDI phase-microscopy system. A = Pinhole; L_0 , L_1 , L_2 = Lenses; BS_1 , BS_2 = Beam splitters; M = Mirror; S = Sample; MO = Microscope objective; (b) Detailed scheme of the sample chamber [11].

3. STANDARD APPROACHES FOR ANALYSIS THE WFDI PHASE PROFILE

3.1 Cells with Homogenous Refractive Index Structure: Single WFDI Exposure \rightarrow Complete Thickness Profile

For homogenous refractive index cells, such as mature RBCs, for which a constant refractive index can be assumed for the entire cell contents, the thickness profile can be directly obtained from the phase profile [13,14]. Figure 2 shows thickness profile of an RBC obtained by WFDI, and the associated thickness scale. In Ref. [10], we have used WFDI to examine the morphology and dynamics of RBCs from individuals who suffer from sickle cell anemia (SCA), a genetic disorder that affects the structure and mechanical properties of RBCs. Using WFDI, we have quantitatively imaged sickle RBCs and measured the nanometer-scale fluctuations in their thickness as an indication of their stiffness. Figure 3(a) presents the quantitative phase profile of the RBCs of a healthy person and Fig. 3(b) presents the RBCs of a person with SCA. As seen in this figure, only a fraction of the sickle RBCs have lost their round-biconcave shape and becomes crescent shaped due to the disease. We have acquired phase profiles of 24 RBCs obtained from two different persons with SCA and 12 RBCs obtained from a healthy person. For each RBC, phase profiles were collected at a frame rate of 120 frames per second during 10 seconds and converted into thickness profiles. For each cell, we have calculated the standard deviation of the thickness fluctuations σ_h , which is inversely proportional to the stiffness map of the RBC [15,16]. Averaging σ_h over the entire RBC area, marked as $\langle \sigma_h \rangle$, yields an indication of the cell flexibility, since less rigid RBCs are expected fluctuate more than stiffer RBCs. Figure 4 presents the quantitative phase profiles and the associated thickness scalebar of two RBCs obtained from a person with SCA. As can be seen in this figure, the right cell has a regular round morphology, whereas the left cell has a crescent morphology. For these sickle RBCs, the standard deviation of the thickness fluctuations averaged over each of the cell areas is $\langle \sigma_h \rangle = 28.73$ nm for the round-morphology RBC and $\langle \sigma_h \rangle = 13.54$ nm for the crescent-morphology RBC. Thus, even though the sickle RBC on the right has a visibly normal morphology, it is found to be more than twice as stiff as the healthy RBC.

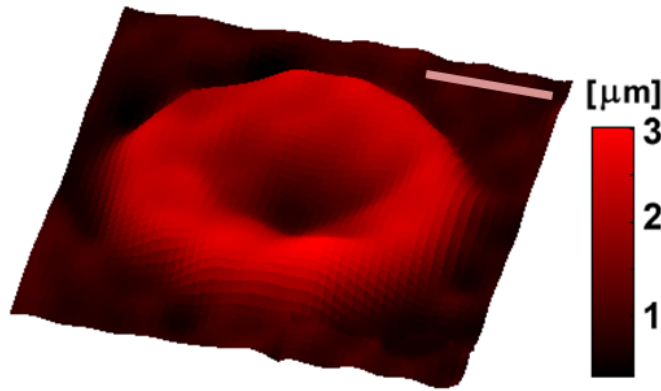


Fig. 2. WFDI quantitative phase profile of a healthy RBC. Scale bar represents 3 μm . Color bar represents thickness in μm [10].

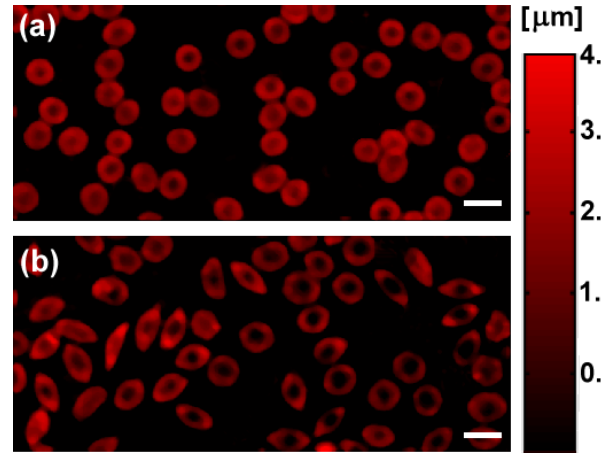


Fig. 3. WFDI quantitative phase imaging of: (a) healthy RBCs, (b) Sickle RBCs, demonstrating the different RBC morphology that characterizes SCA. Quantitative thickness profile can be obtained for each of the cells in the field of view. Scale bar represents 10 μm . Color bar represents thickness in μm [10].

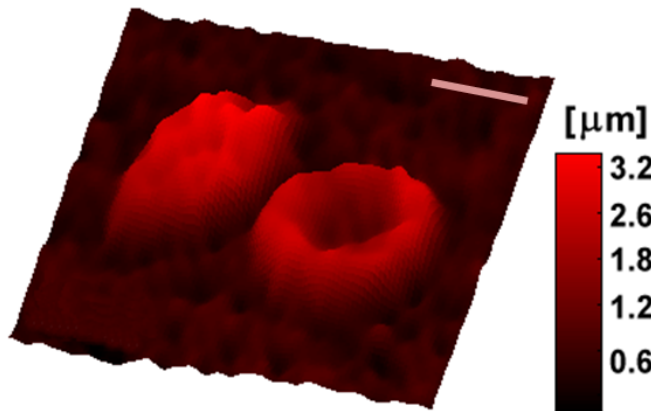


Fig. 4. WFDI quantitative dynamic phase profile of two RBCs obtained from a person with SCA, the right one with round morphology (visibly healthy) and the left one with crescent morphology. The crescent-morphology cell fluctuates less than the round-morphology cell. Scale bar represents 5 μm . Color bar represents thickness in μm [10].

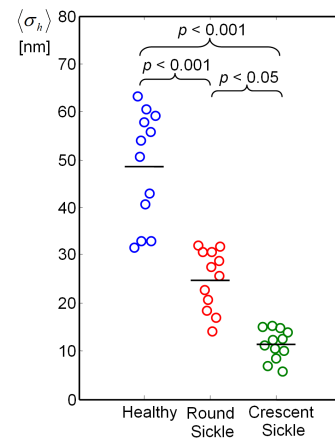


Fig. 5. Averaged standard deviation of RBC thickness fluctuations obtained from the WFDI dynamic phase profiles of RBCs of three groups: round (typical) morphology RBCs from a healthy person, round (visibly healthy) morphology RBCs from a person with SCA, and crescent-morphology RBCs from a person with SCA. Each circle represents a different RBC, and the horizontal line at each group represents the average value of all cells in the group. p -values were calculated by the two-sided Wilcoxon rank-sum test [10].

Figure 5 presents $\langle \sigma_h \rangle$ values obtained for RBCs of three groups: 12 round-morphology RBCs from a healthy person, 12 round-morphology RBCs from two persons with SCA, and 12 crescent-morphology RBCs from two persons with SCA. Each of the two groups of 12 sickle RBCs was composed of 5-7 RBCs from the first person with SCA and 5-7 RBCs from the second person with SCA, where no significant difference was seen between the $\langle \sigma_h \rangle$ values of the RBCs from the two individuals with SCA. The healthy RBCs yielded $\langle \sigma_h \rangle = 51.07 \pm 12.02$ nm, the round-morphology RBCs from SCA individuals yielded $\langle \sigma_h \rangle = 21.76 \pm 7.64$ nm, and the crescent-morphology RBCs from SCA individuals yielded $\langle \sigma_h \rangle = 13.82 \pm 3.92$ nm. These results demonstrate that the healthy RBCs are 2-3 times less stiff than the round-

morphology sickle RBCs, and the latter are approximately half as stiff as the sickle crescent-morphology RBCs. Greater statistical difference, indicated by the lower p -values ($p < 0.001$), is obtained between the group of healthy RBCs and each group of the sickle RBCs than between the two groups of sickle RBCs ($p < 0.05$). The high statistical significance of the difference between the round-morphology RBCs from SCA individuals and the healthy RBCs demonstrates that although the sickle RBC shape might visibly appear to be the same as healthy RBCs, analyzing their thickness fluctuations by WFDI gives a clear indication that they are sickle RBCs. Thus, we have found that sickle RBCs were found to be significantly stiffer than healthy RBCs, and, furthermore, differentiated between sickle RBC morphologies taken from the same subjects by analyzing their thickness fluctuations, where crescent-morphology RBCs are more rigid (fluctuate less) than round-morphology RBCs. We anticipate that this technique will find uses for diagnosis and monitoring of SCA, as well as usefulness as an SCA research tool. In addition to helping identify and prove the effectiveness of new SCA therapeutic approaches, this technique might be useful in differentiating SCA from sickle cell trait, a condition in which there is one gene for the formation of hemoglobin S and one for the formation of normal hemoglobin. Usually, people with sickle cell trait live relatively healthy lives but if their partner has sickle cell trait as well, there is 25% chance that their child will have sickle cell disease. Sickle-trait cells generally do not form sickled cells, and the simplest test for hemoglobin S cannot distinguish between SCA and sickle cell trait.

3.2 Cells with Heterogeneous Refractive Index Structure:

Single WFDI Exposure \rightarrow Dry Mass and Relative Volume

Note, however, that this approach of decoupling cell thickness from refractive index in WFDI phase profiles is limited to homogeneous cell types that do not contain nuclei or other organelles with varying refractive indices. Other studies [17,18] have shown that for heterogeneous cells that contain organelles with different refractive indices, certain parameters such as cell area and dry mass can be obtained directly from the phase profile. Cell area S_c is simply defined as the number of pixels, for which the OPD is above the background OPD, multiplied by the demagnified pixel area. After S_c is known, cell dry mass can be calculated by the following formula:

$$M = \frac{1}{\alpha} \int_{S_c} OPD_c(x, y) ds = \frac{S_c}{\alpha} \langle OPD_c \rangle, \quad (3)$$

where α is the refractive increment constant and can be approximated as 0.18-0.21 ml/g [17], and where $\langle OPD_c \rangle$ is the average OPD over the entire cell area. In a similar way, dry mass surface density can be calculated as follows:

$$\sigma_M(x, y) = \frac{1}{\alpha} OPD_c(x, y). \quad (4)$$

In addition, if the cell volume transiently increases in an isotropic way (for example, due to cell swelling), relative volume can still be calculated in a good approximation. For example, we have shown that cell swelling in articular chondrocytes can be analyzed quantitatively without the need to decouple the thickness from refractive index in the WFDI-based phase measurement [7]. Articular chondrocytes are the cells that compose the cartilage, the connective tissue that distributes mechanical loads between bones and provides almost frictionless surfaces in the joints. The phenotypic expression and metabolic activity of these cells are strongly influenced by shape and volume changes occurring due to mechanical and osmotic stresses. Chondrocytes exhibit rapid swelling or shrinking followed by an active volume recovery in response to osmotic stress. Thus instantaneous evaluation of the chondrocyte volumetric adaptation to such stresses can provide important information on the structure–function relationships in these cells. In Ref. [7], we induced hypoosmotic stress on *in-vitro* chondrocytes by changing the cell medium. Due to the stress, the cells started swelling and ultimately burst. We recorded the dynamic phase profiles of the chondrocytes during this phenomenon by WFDI. Figure 6(a) shows the phase profile of one chondrocyte in the monolayer at three different time points. During cell swelling, the phase profile looks wider and lower. Figure 6(b) shows a two-dimensional view of the phase profiles of several cells in the monolayer, whereas Fig. 6(c) shows a DIC microscopy image of the sample. This demonstrates that the contrast mechanism in DIC microscopy does not yield quantitative information while the contrast in WFDI allows direct quantification of the OPD and various numerical parameters at each spatial point on the cell. In addition, as we have shown in Ref. [7], since WFDI captures the entire wavefront, it is possible to correct for out of focus effects in the sample using only digital Fresnel propagation in post-processing and thus avoiding mechanical sample adjustment. This cannot be done in a non-quantitative technique such as DIC.

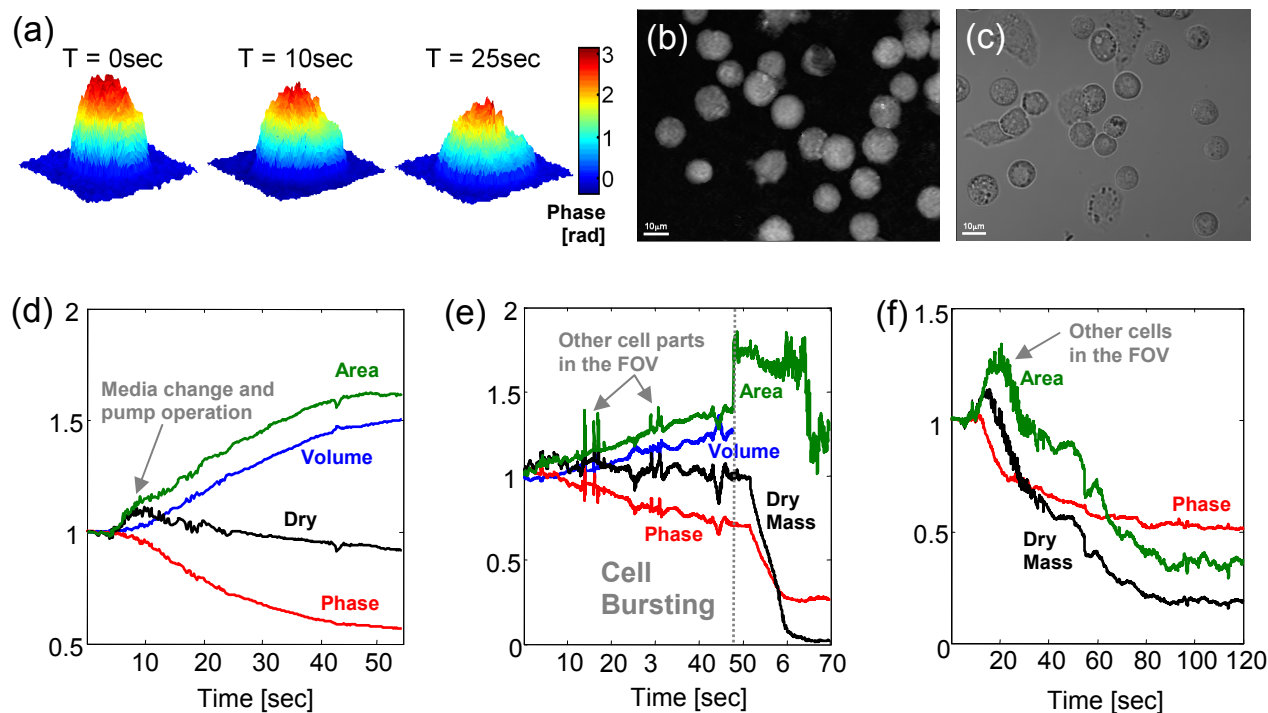


Fig 6. Articular chondrocyte fast dynamics due to hypoosmotic pressure: (a) WFDI-based surface plots of the phase profiles at several different time points; (b) WFDI-based phase profile of the cell monolayer, acquired at 120 frames per second; (c) Phase image of the monolayer obtained by DIC microscopy. (d)-(f) WFDI-based graphs of the relative change in various cell morphological parameters during: (d) single-cell swelling as partially visualized in (a); (e) single-cell swelling and bursting; and (f) cell monolayer dynamics as partially visualized in (b) [7].

Based on these dynamic quantitative WFDI-based phase profiles, we calculated relative volume (according to methods described by Popescu et al. [18] and based on the assumption of isotropic volume change); relative dry mass according to Eq. (3); relative area; and relative average phase. All parameters were calculated as the fractional change from the initial value. Figure 6(d) presents the temporal changes of these parameters during the single-cell hypoosmotic swelling (for the cell illustrated in Fig. 6(a)). As can be seen from these graphs, the chondrocyte volume and area increased by 46% and 52%, respectively, during swelling and maintained an approximately constant dry mass.

Figure 6(e) shows the parameter graphs for the hypoosmotic swelling of another single chondrocyte that gains in volume and area until bursting, at which point its dry mass decreases. This observation provides experimental support of the dry mass calculation that is based on the chondrocyte phase profile (Eq. (3)). The small jumps that can be seen on the graphs before the chondrocyte bursts are further validation of Eq. (3). These jumps correspond exactly to time points at which intracellular debris from other previously burst chondrocytes enter the FOV. Based on the high temporal resolution of our measurements (120 full frames per second), we have calculated the chondrocyte volume just prior to bursting as $V_L=1.28$ times the initial cell volume V_0 . Figure 6(f) shows the time dependence of the relative area, dry mass, and average phase of the cell monolayer visualized in Fig. 6(b). The graphs illustrate the trends in these parameters that occur during the dynamic response of the monolayer. Different chondrocytes start swelling at different time points, swell to various extents, and burst at different time points. Individual cell swelling and bursting results in a decrease in the average phase value. The rupture of an individual cell is characterized by a loss of dry mass and an increase of viewable area until the chondrocyte intracellular debris leaves the FOV. New chondrocytes and intracellular debris entering the FOV result in an increase in dry mass and area. It was demonstrated that the values of all three parameters decrease over time due to the rupture of most chondrocytes in the monolayer. As can also be seen from Fig. 6(f), this results in an approximately uniform distribution of intracellular debris in the chamber [7].

3.3 Cells with Heterogeneous Refractive Index Structure:
Multi WFDI Exposures → Thickness and refractive index profiles

Note that in the chondrocyte experiment, we did not decouple thickness from refractive index since the calculated parameters did not require this operation. If, however, a complete thickness profile is needed, more involved experimental measurements are typically employed. Rappaz et al. [19] used two types of cell media with distinct refractive indices and measured two phase profiles of the same cell. The cell is first measured in the presence of a cell medium with refractive index n_m , yielding a measured cellular OPD of:

$$OPD_{c,1}(x, y) = (\bar{n}_c(x, y) - n_m) \cdot h_c(x, y). \quad (5)$$

Then, the current cell medium is replaced by another cell medium with the same osmolality, to avoid cell volume changes, but with a different refractive index of $n_m + \Delta n$, yielding a cellular OPD of:

$$OPD_{c,2}(x, y) = (\bar{n}_c(x, y) - (n_m + \Delta n_m)) \cdot h_c(x, y). \quad (6)$$

Afterwards, the cell thickness profile can be obtained by subtracting these two equations:

$$h_c(x, y) = \frac{OPD_{c,1}(x, y) - OPD_{c,2}(x, y)}{\Delta n_m}. \quad (7)$$

Using Eq. (7) in any of the two former equations also yields the integral refractive index of the cell as follows:

$$\bar{n}_c(x, y) = \frac{OPD_{c,1}(x, y)\Delta n_m}{OPD_{c,1}(x, y) - OPD_{c,2}(x, y)} + n_m. \quad (8)$$

Despite the simplicity of this two-exposure method, it is effective only if the cell is not highly dynamic and the changes between the consecutive phase measurements are minimal. In other cases, this method is not useful for measuring the correct thickness profile of the cell.

Alternatively, methods of scanning the cell from different points of view can be employed to obtain an intracellular refractive index map [20,21]. Briefly, phase profiles of the cell are measured by WFDI at different angles, by either rotating the sample or changing the illumination direction, and are then processed by a tomographic algorithm (e.g. the filtered backprojection algorithm) to obtain a three-dimensional refractive index map $n_c(x, y, z)$ of the cell. The obtained refractive index map is three-dimensional and not only the integral refractive index $\bar{n}_c(x, y)$ across a plane of view, and thus can be presented slice by slice using any pair of dimensions. This method is more complicated than simple WFDI, since it typically requires mechanical scanning with dedicated hardware, and it also assumes that the cell is static during the scan time; this precludes acquiring three-dimensional refractive index maps of highly dynamic cells by these techniques. Park et al. [22] have proposed a system integrating WFDI and epi-fluorescence microscopy, which can in principle detect organelle locations in real time. If the organelle refractive indices and sizes are known in advance, then the cell thickness profile can be calculated. Rappaz et al. [23] have proposed simultaneous measurement of cell thickness and refractive index by using two illumination wavelengths and a dispersive extracellular dye in the medium.

Alternatively, phase profile measurements can be used in a complementary way: rather than measuring or assuming a certain refractive index and calculating the cell thickness profile, the cell thickness can be measured by another method and then used in combination with the phase measurement obtained by WFDI to calculate the refractive indices of cellular organelles. For example, confocal microscopy has been used in combination with WFDI microscopy to measure refractive indices of cell organelles [24], and cell height measurements obtained by shear-force feedback topography have been combined with WFDI-based phase measurements [25].

Another approach is to obtain the cell thickness by restraining the cell mechanically to a known thickness in the direction perpendicular to the illumination beam. This can be performed, for example, by attaching another coverslip to the sample [26] or using a dedicated micro-channel device [27]. This method, however, applies pressure to the cell and might disturb the behavior of the cell or affect the phenomena of interest.

Kemper et al. [28], Kemmler et al. [29], and Tychinsky et al. [30] have shown that for cells of relatively uniform shape in suspension, the transverse viewable area of the cell can be used to evaluate cell thickness. For example, if the cell shape is a perfect sphere, its width is equal to its height. In all of these specific cases, the integral refractive index can be calculated using the phase profile obtained by WFDI since the cellular thickness is known.

4. NEW APPROACH FOR ANALYSING THE DYNAMIC WFDI PHASE PROFILE

In Ref. [9], we have shown that the WFDI-based phase profiles are useful for quantitative analysis of cells, even in cases where decoupling of thickness and refractive index is not possible or desired. This typically happens for highly-dynamic heterogeneous-refractive-index cells, such as cardiomyocytes (heart muscle cells). By coordinated contraction, these cells control blood flow through the blood vessels of the circulatory system. The dynamic behavior of cardiomyocytes is characterized by a rapid contraction of the cell followed by restoration to equilibrium. Contrary to cells with homogenous refractive index, cardiomyocytes contain organelles with varying refractive indices distributed across the cell interior. These mainly include myofibrils of highly organized sarcomeric arrays of myosin and actin, nuclei, and mitochondria. Using confocal dual-channel fluorescence microscopy, we have demonstrated that the cardiomyocyte organelles of different refractive indices are in motion during the entire beating cycle of the cell [9]. For this reason, it is not possible to accurately decouple refractive index from thickness using the phase-measurement of the entire cardiomyocyte obtained only from single-exposure WFDI. Furthermore, alternative approaches described previously that require more than one exposure (e.g. tomographic scanning or medium-exchange differential measurements; see Section 3.3) can result in loss of dynamic information when recording these cells due to their rapid dynamic nature. This limitation precludes calculating the cell thickness profiles from the phase measurements obtained by single-exposure WFDI during the cell beating cycle. In spite of this fact, we have shown that the dynamic WFDI-base phase profiles of the whole cell are still useful for numerical analysis of the cells [9]. This has been done by identifying certain numerical parameters that quantify specific processes of interest to cell biologists. We have validated the utility of the proposed parameters by showing they are sensitive enough to detect modification of cardiomyocyte contraction dynamics due to temperature change.

In order to numerically quantify the dynamic phase profile of the cells, without the need to extract the thickness profile, we first define the phase-average displacement (PAD) as follows [9]:

$$\Delta\varphi_t(x, y) = \varphi_t(x, y) - \varphi_0(x, y), \quad (9)$$

where $\varphi_t(x, y)$ is the spatially varying phase at time point t , and $\varphi_0(x, y)$ is the spatially varying phase at the resting time point of the cell; if such a time point is not known, $\varphi_0(x, y)$ is defined as the time average of the entire phase-profile $\varphi_0(x, y) = \langle \varphi_t(x, y) \rangle_t$. Using Eq. (9), we define the positive and negative mean-square phase-average displacements (MS-PAD+ and MS-PAD-, respectively) as follows:

$$\Delta\varphi_{MS}^+(x, y) = \left\langle \left(\Delta\varphi_t(x, y) \right)^2 : \Delta\varphi_t(x, y) \geq 0 \right\rangle_t, \quad \Delta\varphi_{MS}^-(x, y) = \left\langle \left(\Delta\varphi_t(x, y) \right)^2 : \Delta\varphi_t(x, y) < 0 \right\rangle_t, \quad (10)$$

and the spectral-domain MS-PAD as follows:

$$\Delta\varphi_{MS}(f_x, f_y) = \left\langle \left| \Delta\varphi_t(f_x, f_y) \right|^2 \right\rangle_t, \quad (11)$$

where $\Delta\varphi_t(f_x, f_y)$ is obtained by a two-dimensional spatial Fourier transform of $\Delta\varphi_t(x, y)$. Using Eqs. (10) and (11), we define the following parameters to describe the MS-PAD global contributions:

$$\eta_1^+ = \sqrt{\langle \Delta\varphi_{MS}^+(x, y) \rangle_{(x, y)}}, \quad \eta_1^- = \sqrt{\langle \Delta\varphi_{MS}^-(x, y) \rangle_{(x, y)}}, \quad \eta_2 = \sqrt{\langle \Delta\varphi_{MS}(f_x, f_y) \rangle_{(f_x, f_y)}}, \quad (12)$$

where $\langle \bullet \rangle_{(x, y)}$ and $\langle \bullet \rangle_{(f_x, f_y)}$ define an area averaging.

Let us also define the phase instantaneous displacement (PID) as follows:

$$\Delta\varphi_{t, \tau}(x, y) = \varphi_{t+\tau}(x, y) - \varphi_t(x, y). \quad (13)$$

where τ defines the time duration between time point t and time point $t + \tau$. Using Eq. (13), we define the positive and negative mean-square phase instantaneous displacements (MS-PID+ and MS-PID-, respectively) as follows:

$$\Delta\varphi_{MS, \tau}^+(x, y) = \langle (\Delta\varphi_{t, \tau}(x, y))^2 : \Delta\varphi_{t, \tau}(x, y) \geq 0 \rangle_t, \quad \Delta\varphi_{MS, \tau}^-(x, y) = \langle (\Delta\varphi_{t, \tau}(x, y))^2 : \Delta\varphi_{t, \tau}(x, y) < 0 \rangle_t, \quad (14)$$

as well as the spectral-domain MS-PID as follows:

$$\Delta\varphi_{MS, \tau}(f_x, f_y) = \langle |\Delta\varphi_{t, \tau}(f_x, f_y)|^2 \rangle_t, \quad (15)$$

where $\Delta\varphi_{t, \tau}(f_x, f_y)$ is obtained by a spatial Fourier transform of $\Delta\varphi_{t, \tau}(x, y)$. By using Eqs. (14) and (15), we define parameters describing the MS-PID global contributions:

$$\gamma_{1, \tau}^+ = \sqrt{\langle \Delta\varphi_{MS, \tau}^+(x, y) \rangle_{(x, y)}}, \quad \gamma_{1, \tau}^- = \sqrt{\langle \Delta\varphi_{MS, \tau}^-(x, y) \rangle_{(x, y)}}, \quad \gamma_{2, \tau} = \sqrt{\langle \Delta\varphi_{MS, \tau}(f_x, f_y) \rangle_{(f_x, f_y)}}. \quad (16)$$

Since the cell phase profile is strongly associated with its dry mass [17,18], the parameters defined above are associated with motion of different intracellular structures including organelles. Note that these parameters are based on the entire dynamic phase profile, without the need to first extract the physical thickness profile.

The analysis tools described above are sensitive enough to detect the subtle changes in the dynamic phase profile of a beating cardiomyocyte [9]. Figures 7(a) and (e) compare the phase profiles a cardiomyocyte during a single beating cycle at 30°C and 23°C, respectively. The cell in Fig. 7(e) tends to show more motion along a greater portion of its length in comparison to the cell shown in Fig. 7(a), especially in the recovery stage (defined as the time interval between the point of maximum stretch of the cell and the point when the cell returned to the resting stage). The relatively slow recovery phase observed at lower temperatures is consistent with temperature-induced inhibition of calcium-regulated contraction, as discussed at the end of this section. The dynamic differences during the beating cycle of the same cell at 30°C in comparison to 23°C are more obvious from the PAD and PID profiles shown in Figs. 7(b-d, f-h) (also see Media 4 in Ref. [9]). As seen in Figs. 7(b, f), the PAD profiles of cardiomyocytes provide a means of tracking the differential changes in the current WFDI phase profile compared to the associated phase profile in the cell resting point (defined by Eq. (9)), which reveals the dry-mass movement inside the cell. Thus the PAD profiles can be used to study cell function during the beating cycle. Furthermore, the global contribution of the dynamic PAD profiles characterizes the entire beating cell cycle and is the basis for the MS-PAD profiles, which are described by the single-value η parameters. As can be seen in Fig. 7(c, d, g, h), the PID profiles give an indication of the instantaneous movement of dry mass in the cell associated with organelles of different sizes over different time periods during the cell beating cycle, as defined by the time parameter τ . The subtraction operation defined by Eq. (13) creates a differential measurement between the current phase profile and a previous phase profile that is time-shifted by τ . Phase contributions from this previous frame are thus canceled and the uncorrelated regions between the two frames are revealed. The MS-PID profiles are calculated based on the dynamic PID profiles, yielding the single-valued γ parameters characterizing the cell over various time periods during the experiment.

The numerical analysis described above was performed on the WFDI phase profiles of 18 individual cardiomyocytes at 30°C and at 23°C [9]. The values obtained for each of the γ and η parameters were averaged over 3-4 beating cycles and normalized by the viewable area of the cell. Statistical significance between the two groups of cells (at 30°C and at 23°C) were seen for all γ and η parameters as indicated by low p -values, which were calculated by the two-sided Wilcoxon rank-sum test [31]. These results demonstrate that the unique whole-cell-based numerical parameters defined in Ref. [9] can be used to discriminate between different dynamic behaviors of cardiomyocytes, and thus can be used to quantitatively study dynamic phenomena in these cells.

As can also be seen in Fig. 8, there is an apparent advantage for using the negative parameters $\gamma_{1,\tau}^-$ for discriminating between the two groups of cells. Higher values in these parameters represent increased levels of MS-PID-. In the recovery phase of the cell, it is more likely to have more cell points with negative MS-PID than positive MS-PID, since the phase profile in the cell contractile region decreases. This implies that there is a larger influence of the ambient temperature in the recovery phase of the cell beating, as compared to the contraction phase. These results are supported by previous studies performed by other methods, where temperature had a profound effect on the biochemistry of contraction in the myocardium of the intact heart and in cardiomyocytes *in vitro* [32].

The whole-cell analysis tools presented here capture intermediate events associated with dry mass movement over different time scales during the cardiomyocyte beating cycle. These intermediate events cannot be well discriminated by directly visualizing the dynamic phase profiles of the cell. In contrast, the single-valued η and γ parameters can uniquely characterize cell function, as demonstrated for temperature change. We believe that these numerical tools will be useful for analyzing various fast dynamic behaviors in other biological cells, including intracellular and extracellular membrane fluctuations and reorganization of the cell cytoskeleton. More details on this subject can be found in Ref. [9].

5. CONCLUSION

We have presented the principle of WFDI phase microscopy for quantitative holographic imaging of biological cells. The WFDI-based phase profiles can then be simply converted to OPD profiles, which contain the coupled specimen refractive index and physical thickness. We have shown that for homogeneous refractive-index-structure cells such as RBCs, the OPD profile is proportional to the thickness profile and thus stiffness maps can be calculated. For heterogeneous cells, dry mass can be directly calculated from the OPD profile. As demonstrated for cell swelling in chondrocytes, relative volume can be calculated as well under an assumption of isotropic volume change.

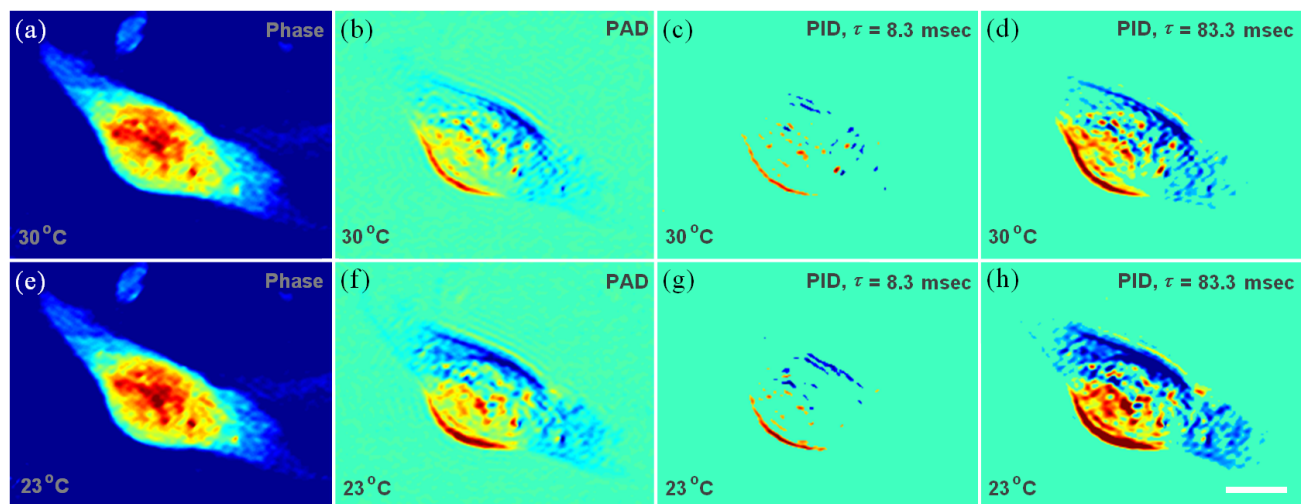


Fig. 7. Example of numerical analysis applied on a WFDI phase profile of a cardiomyocyte during beating at two different temperatures: (a-d) at 30°C, (e-h) at 23°C. (a,e) Phase profile; (b,f) PAD profile; (c,g) PID profile for $\tau = 8.3$ msec; (d,h) PID profile for $\tau = 83.3$ msec. In (b-d,f-h): ‘hot’ colors represent positive values, ‘cold’ colors represent negative values, and cyan represents zeros. White horizontal scale bar represents 10 μm [6]. Dynamics, 120 fps for 1 sec: see Media 4 in Ref. [9].

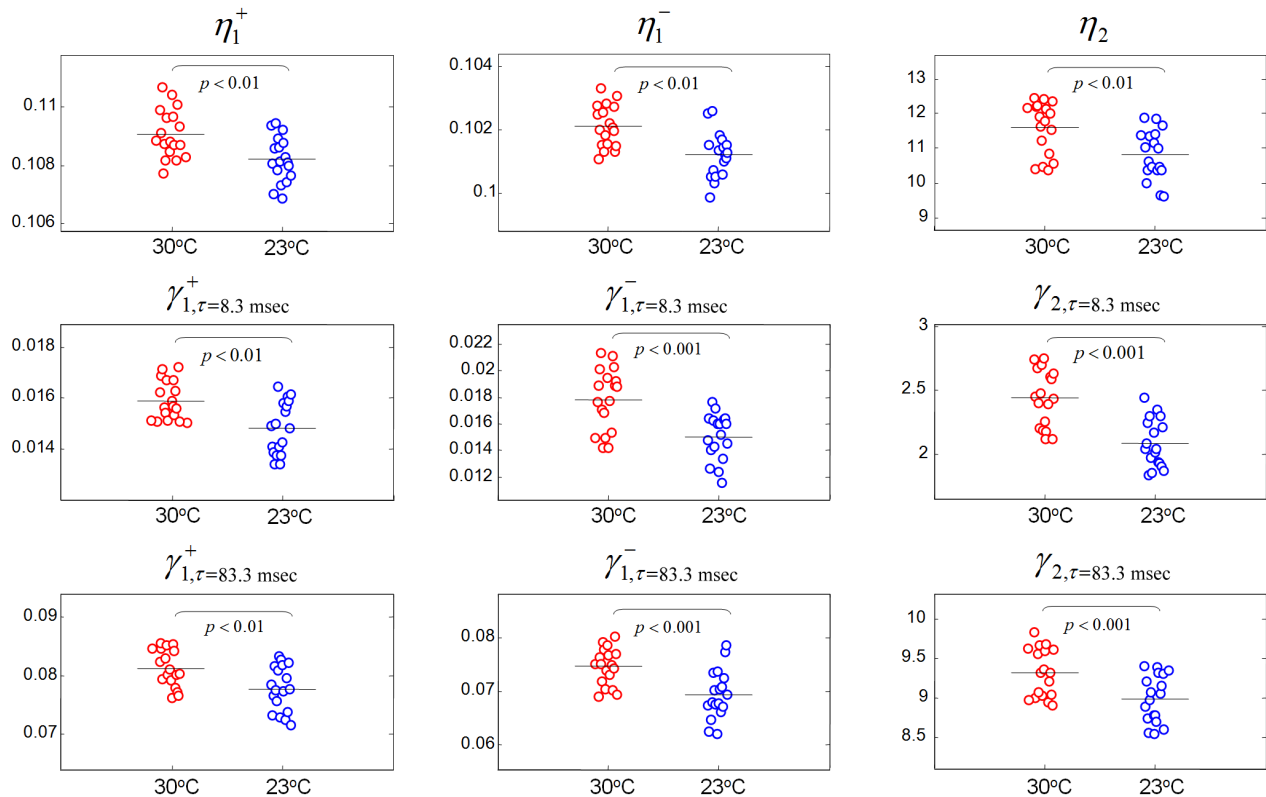


Fig. 8. Values of the γ and η parameters that are based on the whole-cell phase profiles, demonstrating that these parameters discriminate between cardiomyocytes beating at 30°C and 23°C (18 cells in each group, 3-4 beating cycles per each cell). Each circle represents a different cardiomyocyte, and the horizontal line at each group represents the average value for all cells in the group [9].

Several other systems made use of multiple measurements at varying angular projections, immersion media, or wavelengths in an attempt to decouple refractive index from thickness. However, these techniques trade off system complexity and temporal measurements in order to extract these coupled parameters.

Finally, we have introduced whole-cell analysis approach that uses differential phase profiles referenced to either an initial physiological or time-averaged state (phase-average displacement, PAD) or a finite time delay (phase-instantaneous displacement, PID). Examining the mean-square PAD and PID over the course of a dynamic experiment provides information about the motion of intracellular organelles. Based on these profiles, we have calculated the parameters γ and η that can uniquely characterize dynamic cells measured by WFDI. These new parameters have been shown to be effective at discriminating dynamic cellular behavior of beating cardiomyocytes as influenced by temperature.

WFDI phase microscopy has been shown to be highly effective for quantitative analysis of rapid cellular dynamics without the need for special sample preparation, and thus this technique has a significant potential for unique characterization of various cellular phenomena and diseases.

ACKNOWLEDGMENTS

The experiments presented in this paper were performed while N.T.S. was visiting in the Department of Biomedical Engineering in Duke University. These experiments were financially supported by National Science Foundation (NSF) grants CBET-0651622 and MRI-1039562, as well as the Bikura Postdoctoral Fellowship from Israel.

REFERENCES

- [1] Cuche, E., Marquet, P. and Depeursinge, C., "Simultaneous amplitude-contrast and quantitative phase-contrast microscopy by numerical reconstruction of Fresnel off-axis holograms," *Appl. Opt.* 38, 6994-7001 (1999).
- [2] Marquet, P., Rappaz, B., Magistretti, P.J., Cuche, E., Emery, Y., Colomb, T. and Depeursinge, C., "Digital holographic microscopy: a noninvasive contrast imaging technique allowing quantitative visualization of living cells with subwavelength axial accuracy," *Opt. Lett.* 30, 468-470 (2005).
- [3] Ikeda, T., Popescu, G., Dasari, R. R. and Feld, M. S., "Hilbert phase microscopy for investigating fast dynamics in transparent systems," *Opt. Lett.* 30, 1165-1167 (2005).
- [4] Shaked, N. T., Rinehart, M. T. and Wax, A., "Dual-interference-channel quantitative-phase microscopy of live cell dynamics," *Opt. Lett.* 34, 767-769 (2009).
- [5] Shaked, N. T., Zhu, Y., Rinehart, M. T. and Wax, A., "Two-step-only phase-shifting interferometry with optimized detector bandwidth for microscopy of live cells," *Opt. Express* 17, 15585-15591 (2009).
- [6] Shaked, N. T., Newpher, T. M., Ehlers, M. D. and Wax, A., "Parallel on-axis holographic microscopy of biological cells and unicellular micro-organism dynamics," *Appl. Opt.* 49, 2872-2878 (2010).
- [7] Shaked, N. T., Finan, J. D., Guilak, F. and Wax, A., "Quantitative phase microscopy of articular chondrocyte dynamics by wide-field digital interferometry," *J. Biomed. Opt. Lett.* 15, 010505 (2010).
- [8] Shaked, N. T., Zhu, Y., Badie, N., Bursac, N. and Wax, A., "Reflective interferometric chamber for quantitative phase imaging of biological sample dynamics," *J. Biomed. Opt. Lett.* 15, 030503 (2010).
- [9] Shaked, N. T., Satterwhite, L. L., Bursac, N. and Wax, A., "Whole cell analysis of live cardiomyocytes using wide-field interferometric phase microscopy," *Biomed. Opt. Express* 1, 706-719 (2010).
- [10] Shaked, N. T., Satterwhite, L. L., Truskey, G. A., Telen, M. J. and Wax, A., "Quantitative microscopy and nanoscopy of sickle red blood cells performed by wide field digital interferometry," *J. of Biomed. Opt. Lett.* 16, 030506 (2011).
- [11] Shaked, N. T., Satterwhite, L. L., Rinehart, M. T. and Wax, A., "Quantitative analysis of biological cells using digital holographic microscopy," in [Holography, Research and Technologies], INTECH (2011).
- [12] Rappaz, B., Marquet, P., Cuche, E., Emery, Y., Depeursinge, C. and Magistretti, P., "Measurement of the integral refractive index and dynamic cell morphometry of living cells with digital holographic microscopy," *Opt. Express* 13, 9361-9373 (2005).
- [13] Popescu, G., Ikeda, T., Badizadegan, K., Dasari, R. R. and Feld, M. S., "Erythrocyte structure and dynamics quantified by Hilbert phase microscopy," *J. Biomed. Opt. Lett.* 10, 060503 (2005).
- [14] Rappaz, B., Barbul, A., Emery, Y., Korenstein, R., Depeursinge, C., Magistretti, P. J. and Marquet, P., "Comparative study of human erythrocytes by digital holographic microscopy, confocal microscopy, and impedance volume analyzer," *Cytometry* 73A, 895-903 (2008).
- [15] Popescu, G., Park, Y. K., Choi, W., Dasari, R. R., Feld, M. S. and Badizadegan, K., "Imaging red blood cell dynamics by quantitative phase microscopy," *Blood Cells, Molecules, and Diseases* 41, 10-16 (2008).
- [16] Park, Y. K., Best, C. A., Auth, T., Gov, N. S., Safran, S. A., Popescu, G. and Suresh, S., "Metabolic remodeling of the human red blood cell membrane," *Proc. Natl. Acad. Sci. USA* 107, 1289-1294 (2010).
- [17] Barer, R., "Interference microscopy and mass determination," *Nature* 169, 366-367 (1952).
- [18] Popescu, G., Park, Y. K., Lue, N., Best-Popescu, C. A., Deflores, L., Dasari, R. R., Feld, M. S. and Badizadegan, K., "Optical imaging of cell mass and growth dynamics," *The American Journal of Physiology - Cell Physiology* 295, C538-C544 (2008).
- [19] Rappaz, B., Marquet, P., Cuche, E., Emery, Y., Depeursinge, C. and Magistretti, P., "Measurement of the integral refractive index and dynamic cell morphometry of living cells with digital holographic microscopy," *Opt. Express* 13, 9361-9373 (2005).
- [20] Charrière, F., Marian, A., Montfort, F., Kuehn, J., Colomb, T., Cuche, E., Marquet, P. and Depeursinge, C., "Cell refractive index tomography by digital holographic microscopy," *Opt. Lett.* 31, 178-180 (2006).
- [21] Choi, W., Fang-Yen, C., Badizadegan, K., Oh, S., Lue, N., Dasari, R. R. and Feld, M. S., "Tomographic phase microscopy," *Nature Methods* 4, 717-719 (2007).
- [22] Park, Y. K., Popescu, G., Badizadegan, K., Dasari, R. R. and Feld, M. S., "Diffraction phase and fluorescence microscopy," *Opt. Express* 14, 8263-8268 (2006).

- [23] Rappaz, B., Charrière, F., Depeursinge, C., Magistretti, P. J. and Marquet, P., "Simultaneous cell morphometry and refractive index measurement with dual-wavelength digital holographic microscopy and dye-enhanced dispersion of perfusion medium," *Opt. Lett.* 33, 744-746 (2008).
- [24] Curl, C. L., Bellair, C. J., Harris, T., Allman, B. E., Harris, P. J., Stewart, A. G., Roberts, A., Nugent, K. A. and Delbridge, L. M., "Refractive index measurement in viable cells using quantitative phase-amplitude microscopy and confocal microscopy," *Cytometry* 65A, 88-92 (2005).
- [25] Edward, K., Farahi, F. and Hocken, R., "Hybrid shear force feedback/scanning quantitative phase microscopy applied to subsurface imaging," *Opt. Express* 17, 18408-18418 (2009).
- [26] Kemper, B., Carl, D., Schnekenburger, J., Bredebusch, I., Schafer, M., Domschke, W. and von Bally, G., "Investigation of living pancreas tumor cells by digital holographic microscopy," *J. Biomed. Opt.* 11, 34005 (2006).
- [27] Lue, N., Popescu, G., Ikeda, T., Dasari, R. R., Badizadegan, K. and Feld, M. S., "Live cell refractometry using microfluidic devices," *Opt. Lett.* 31, 2759-2761 (2006).
- [28] Kemper, B., Kosmeier, S., Langehanenberg, P., von Bally, G., Bredebusch, I., Domschke, W. and Schnekenburger, J., "Integral refractive index determination of living suspension cells by multifocus digital holographic phase contrast microscopy," *J. Biomed. Opt.* 12, 054009 (2007).
- [29] Kemmler, M., Fratz, M., Giel, D., Saum, N., Brandenburg, A. and Hoffmann, C., "Non-invasive time-dependent cytometry monitoring by digital holography," *J. Biomed. Opt.* 12, 064002 (2006).
- [30] Tychinsky, V. P., Kretushev, A. V., Klemiyashov, I. V., Vyshenskaya, T. V., Filippova, N. A., Raikhlin, N. T. and Shtil, A. A., "Quantitative real-time analysis of nucleolar stress by coherent phase microscopy," *J. Biomed. Opt.* 13, 064032 (2008).
- [31] Conover, W. J., [Practical Nonparametric Statistics, 3rd Edition], John Wiley, pp. 271-276 (1999).
- [32] Fu, Y., Zhang, G.-Q., Hao, X.-M., Wu, C.-H., Chai, Z. and Wang, S.-Q., "Temperature dependence and thermodynamic properties of Ca²⁺ sparks in rat cardiomyocytes," *Biophysical Journal* 89, 2533-2541 (2005).